

# Basic electronic properties of iron selenide under variation of structural parameters

Daniel Guterding,<sup>1,\*</sup> Harald O. Jeschke,<sup>2</sup> and Roser Valentí<sup>1</sup>

<sup>1</sup>*Institut für Theoretische Physik, Goethe-Universität Frankfurt,  
Max-von-Laue-Straße 1, 60438 Frankfurt am Main, Germany*

<sup>2</sup>*Research Institute for Interdisciplinary Science, Okayama University, Okayama 700-8530, Japan*

Since the discovery of high-temperature superconductivity in the thin-film FeSe/SrTiO<sub>3</sub> system, iron selenide and its derivatives have been intensively scrutinized. Using *ab initio* density functional theory calculations we review the electronic structures that could be realized in iron-selenide if the structural parameters could be tuned at liberty. We calculate the momentum-dependence of the susceptibility and investigate the symmetry of electron pairing within the random phase approximation. Both the susceptibility and the symmetry of electron pairing depend on the structural parameters in a nontrivial way. These results are consistent with the known experimental behavior of binary iron chalcogenides and, at the same time, reveal two promising ways of tuning superconducting transition temperatures in these materials. On the one hand by expanding the iron lattice of FeSe at constant iron-selenium distance and, on the other hand, by increasing the iron-selenium distance with unchanged iron lattice.

## I. INTRODUCTION

Since the discovery of iron based superconductors in 2008, this field has matured, with many efforts going into tuning properties of the materials towards higher transition temperatures, higher critical fields, better crystal properties, or less rare constituents. The iron chalcogenides with its primary exponent FeSe<sup>1,2</sup> have recently attracted intense scrutiny. On the one hand, there are experimental facts like the large nematic region<sup>3</sup> that continue to trigger theoretical efforts<sup>4-9</sup> in the hope of improving and unifying our understanding of iron based superconductors in general. On the other hand, special types of tuning like growth on substrates<sup>10-12</sup>, doping<sup>13-18</sup> intercalation<sup>19-26</sup>, and the family of alkali iron chalcogenides<sup>27</sup> make FeSe and its derivatives especially rich. There have been several attempts to identify crucial tuning properties in FeSe, in particular the Se height<sup>28,29</sup> or the doping level.

The tetragonal FeSe crystal structure is intriguingly simple; it is fully specified by  $a$  and  $c$  lattice parameters and the  $z$  coordinate. However, focusing more closely on a single layer of FeSe, it is clear that the electronic structure is controlled by only two geometric parameters, the Fe-Fe distance  $d_{\text{Fe-Fe}}$  which is identical to the  $a$  lattice parameter divided by  $\sqrt{2}$ , and the Fe-Se distance  $d_{\text{Fe-Se}}$ . Experimentally, a large range of these two distances  $d_{\text{Fe-Fe}}$  and  $d_{\text{Fe-Se}}$  can be realized using pressure<sup>30,31</sup>, strain<sup>32</sup>, substrates<sup>10,33,34</sup>, intercalation<sup>19-22,24-26</sup>, chalcogenide substitution<sup>13-18</sup> and charge doping<sup>35</sup>.

In this contribution, we intend to scan the possible electronic structures that could be realized if  $d_{\text{Fe-Fe}}$  and  $d_{\text{Fe-Se}}$  could be tuned at liberty. This is done with the hope of identifying promising directions in the  $(d_{\text{Fe-Fe}}, d_{\text{Fe-Se}})$  parameter space which could then be targeted by material design efforts. For the present study, we intentionally leave out the other significant tuning axis which is the filling of the Fe bands; we fix it to the charge of the neutral FeSe layer. We then survey as function

of  $(d_{\text{Fe-Fe}}, d_{\text{Fe-Se}})$  the variability of the FeSe electronic structure, Fermi surface, essential tight binding parameters, magnetic susceptibility, as well as pairing symmetry and strength. We note that in this study we will neither handle nematicity nor enter into the discussion of correlation effects<sup>36-39</sup>, but we will rather concentrate on the basic trends of the electronic properties.

Our main observations are: (i) Expansion of the Fe square lattice parameter at constant Fe-Se distance  $d_{\text{Fe-Se}}$  should enhance  $T_c$  up to a point before a switch

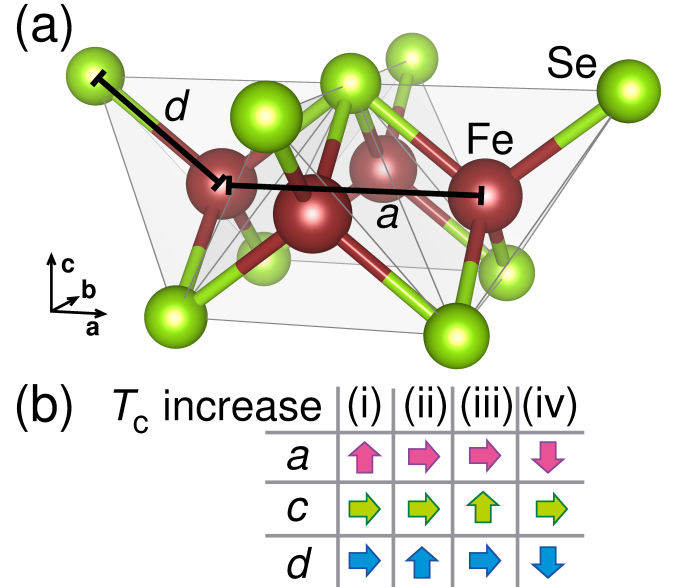


FIG. 1. (Color online) Crystal structure of FeSe (top) and summary of the four ways to increase the superconducting transition temperature  $T_c$  (bottom) by changing lattice parameters  $a$ ,  $c$  and  $d$ , as described in the main text. Arrows indicate the change in lattice parameter. An up arrow represents enlargement, a down arrow represents shrinking, while a horizontal arrow represents keeping the parameter unchanged compared to the experimental pristine FeSe.

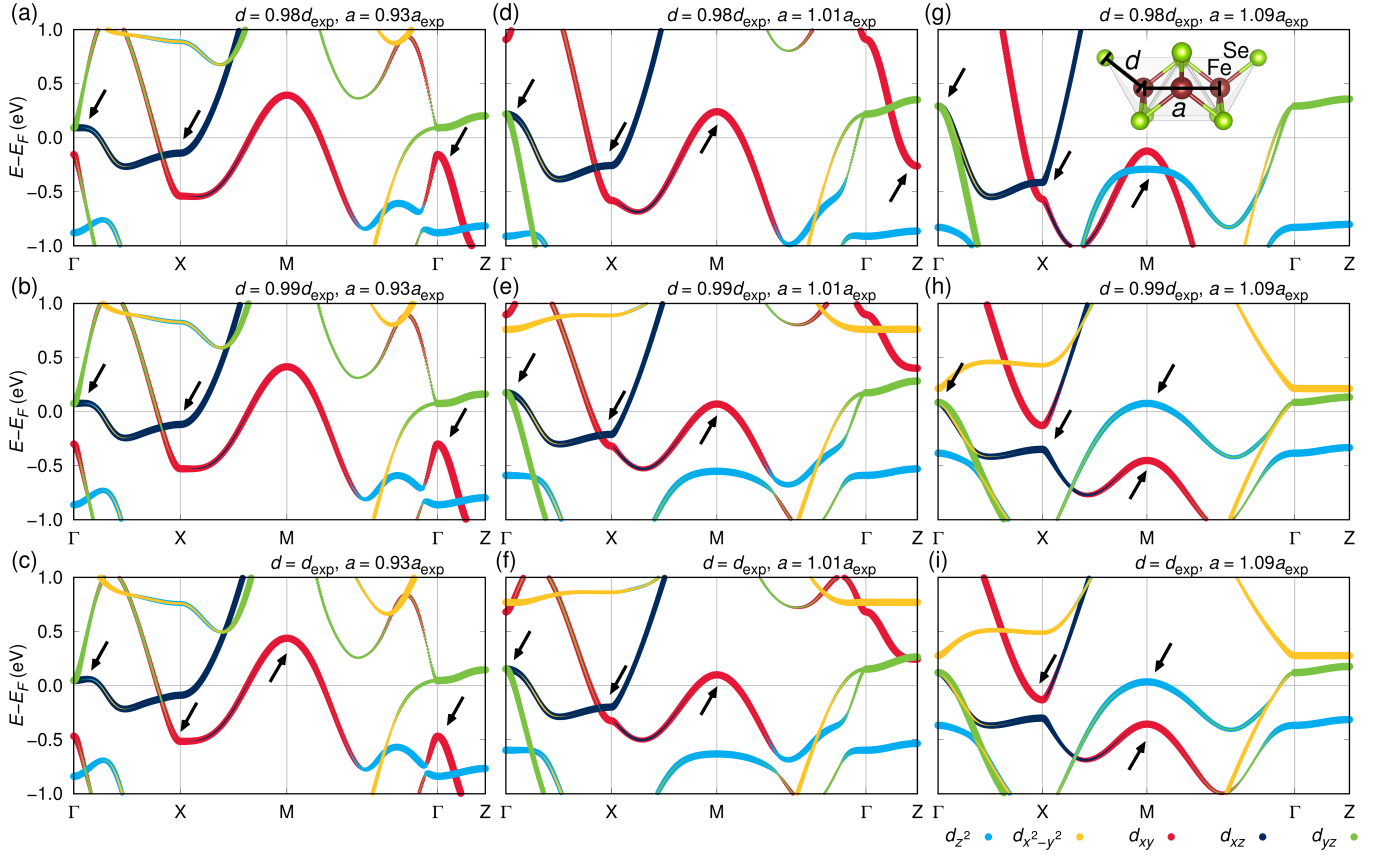


FIG. 2. (Color online) Electronic bandstructure with orbital weights indicated by colors for varied iron-selenium distance  $d_{\text{Fe-Se}}$  and lattice parameter  $a$ . (a)-(c)  $a = 3.5 \text{ \AA} = 0.93a_{\text{exp}}$ , (d)-(f)  $a = 3.8 \text{ \AA} = 1.01a_{\text{exp}}$  and (g)-(i)  $a = 4.1 \text{ \AA} = 1.09a_{\text{exp}}$ . First row (a), (d), (g)  $d_{\text{Fe-Se}} = 2.35 \text{ \AA} = 0.98d_{\text{exp}}$ , second row (b), (e), (h)  $d_{\text{Fe-Se}} = 2.37 \text{ \AA} = 0.99d_{\text{exp}}$  and third row (c), (f), (i)  $d_{\text{Fe-Se}} = 2.393 \text{ \AA} \equiv d_{\text{exp}}$ . Arrows mark points where changes in the bandstructure happen as a function of parameters.

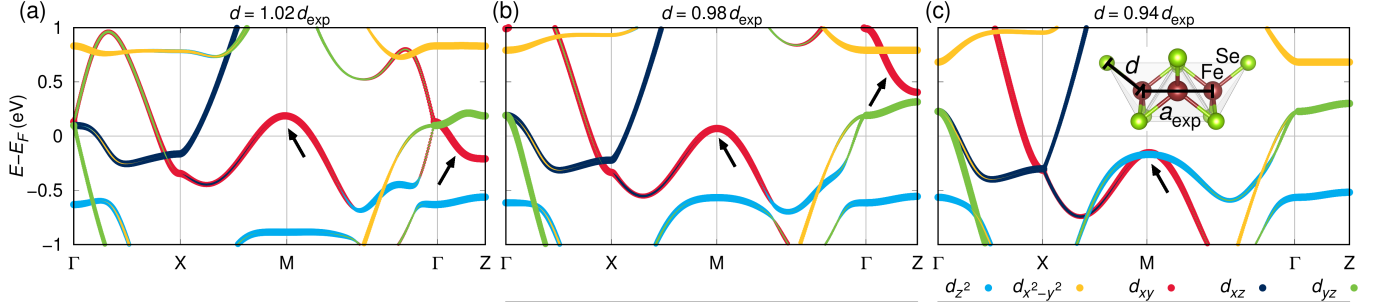


FIG. 3. (Color online) Electronic bandstructure with orbital weights indicated by colors at constant lattice parameter  $a = a_{\text{exp}}$  and varied iron-selenium distance  $d$ . (a)  $d_{\text{Fe-Se}} = 2.447 \text{ \AA} = 1.02d_{\text{exp}}$ , (b)  $d_{\text{Fe-Se}} = 2.348 \text{ \AA} = 0.98d_{\text{exp}}$  and (c)  $d_{\text{Fe-Se}} = 2.256 \text{ \AA} = 0.94d_{\text{exp}}$ . Arrows mark points where changes in the bandstructure happen as a function of parameters.

of superconducting order parameter from  $s_{\pm}$  to  $d_{x^2-y^2}$  occurs. (ii) Alternatively, increasing the Fe-Se distance at constant Fe square lattice parameter  $a$  should also enhance  $T_c$ . Furthermore, (iii) increasing the  $c$  lattice parameter at constant experimental  $d_{\text{Fe-Fe}}$  and  $d_{\text{Fe-Se}}$  distances (i.e. increasing the van der Waals gap) only slightly increases  $T_c$ , while (iv) compression of the Fe-Fe square lattice at slightly compressed Fe-Se distance significantly enhances  $T_c$ . Observation (iii) is essentially

known from charge neutral FeSe intercalates and observation (iv) is very consistent with the well known pressure enhancement of  $T_c$ . However, observations (i) and (ii) could lead to new design ideas. A summary of our findings is given in Fig. 1.

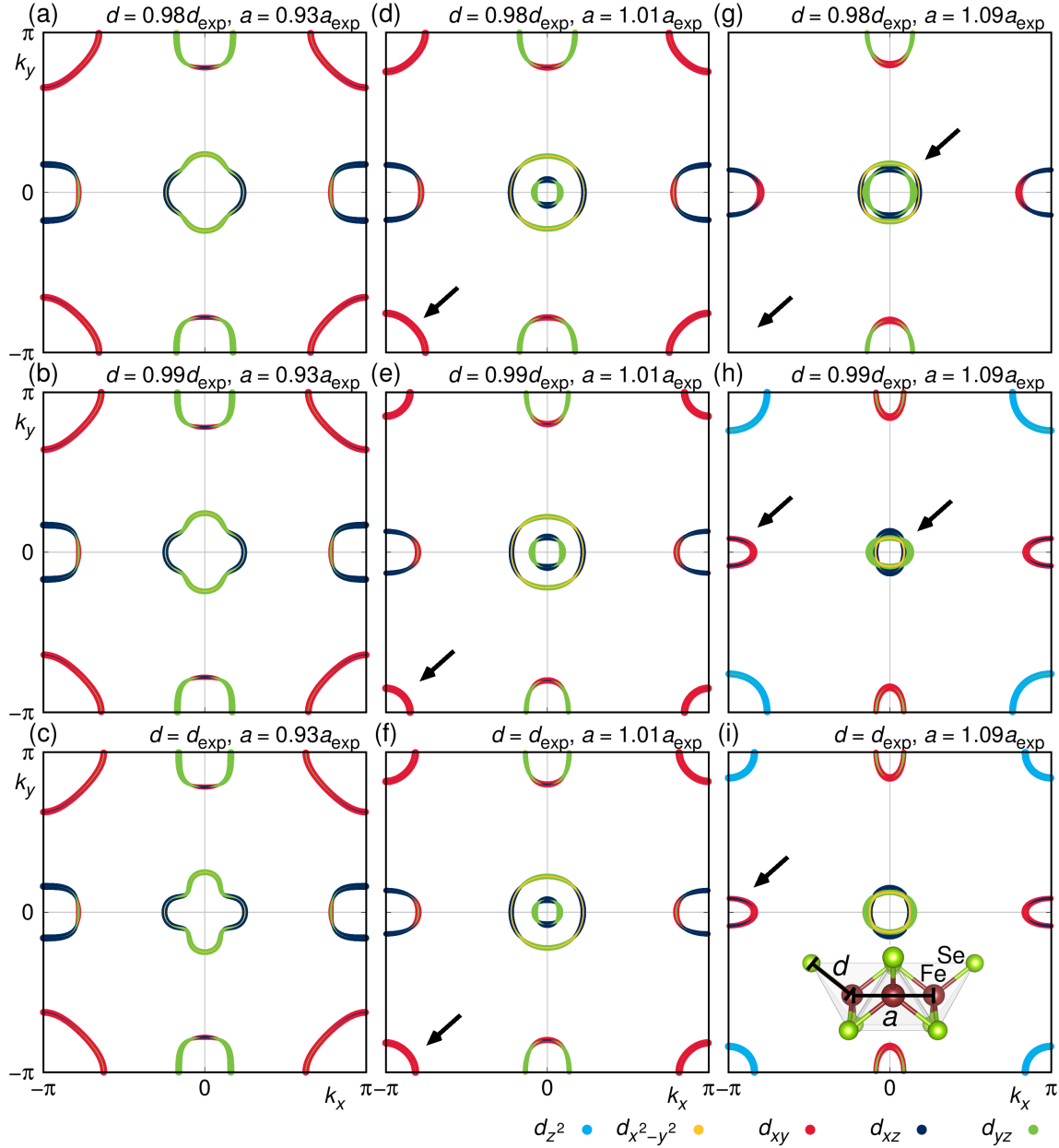


FIG. 4. (Color online) Fermi surface with orbital weights indicated by colors for varied iron-selenium distance  $d_{\text{Fe-Se}}$  and lattice parameter  $a$ . (a)-(c)  $a = 3.5 \text{ \AA} = 0.93a_{\text{exp}}$ , (d)-(f)  $a = 3.8 \text{ \AA} = 1.01a_{\text{exp}}$  and (g)-(i)  $a = 4.1 \text{ \AA} = 1.09a_{\text{exp}}$ . First row (a), (d), (g)  $d_{\text{Fe-Se}} = 2.35 \text{ \AA} = 0.98d_{\text{exp}}$ , second row (b), (e), (h)  $d_{\text{Fe-Se}} = 2.37 \text{ \AA} = 0.99d_{\text{exp}}$  and third row (c), (f), (i)  $d_{\text{Fe-Se}} = 2.393 \text{ \AA} \equiv d_{\text{exp}}$ . Arrows mark points where changes in the Fermi surface happen as a function of parameters.

## II. METHODS AND MODELS

### A. *Ab initio* calculations and model construction

As a starting point for our calculations we use the  $^{56}\text{FeSe}_{1-x}$  structure in space group  $P4/\text{nm}$  (No. 129) obtained at  $T = 250 \text{ K}$  in Ref. 40. The structural parameters are  $a = 3.76988 \text{ \AA} \equiv a_{\text{exp}}$ ,  $c = 5.51637 \text{ \AA} \equiv c_{\text{exp}}$  and  $d_{\text{Fe-Se}} = 2.393 \text{ \AA} \equiv d_{\text{Fe-Se exp}}$ .

To investigate the dependence of the electronic struc-

ture on these parameters, we modify the crystal structures manually and calculate the electronic bandstructure using density functional theory (DFT) within the full-potential local orbital (FPLO)<sup>41</sup> basis independently for each case. We use the generalized gradient approximation<sup>42</sup> for the exchange-correlation functional. All calculations were converged on  $20 \times 20 \times 20$   $\mathbf{k}$ -point grids.

Tight-binding models were constructed using projective Wannier functions<sup>43</sup>. The energy window chosen for the projection spans approximately from -2.5 eV to 2.0 eV. We include all Fe  $3d$  states, which yields a ten-

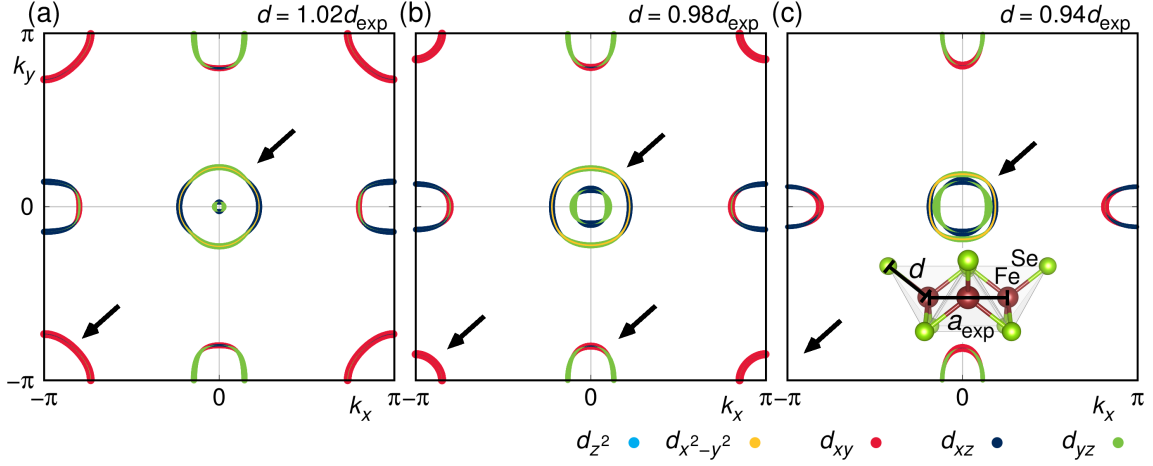


FIG. 5. (Color online) Fermi surface with orbital weights indicated by colors at constant lattice parameter  $a = a_{\text{exp}}$  and varied iron-selenium distance  $d$ . (a)  $d_{\text{Fe-Se}} = 2.447 \text{ \AA} = 1.02d_{\text{exp}}$ , (b)  $d_{\text{Fe-Se}} = 2.348 \text{ \AA} = 0.98d_{\text{exp}}$  and (c)  $d_{\text{Fe-Se}} = 2.256 \text{ \AA} = 0.94d_{\text{exp}}$ . Arrows mark points where changes in the Fermi surface happen as a function of parameters.

orbital model for the electronic structure, since the crystallographic unit cell contains two formula units of FeSe. Using the recently developed glide reflection unfolding technique<sup>44</sup>, these ten-orbital models are reduced to five-orbital models for an effective one-iron unit cell. The calculated hopping parameters are denoted as  $t_{ij}^{sp}$ , where  $i$  and  $j$  are lattice site indices and indices  $s$  and  $p$  identify the orbitals.

$$H_0 = - \sum_{i,j,s,p,\sigma} t_{ij}^{sp} c_{is\sigma}^\dagger c_{jp\sigma} \quad (1)$$

The five-orbital models constitute the kinetic part of the full model Hamiltonian under investigation. Since the bandstructure calculated from DFT and the subsequently obtained tight-binding models are virtually identical in the energy window of interest, we use from now on only the tight-binding representation.

## B. Susceptibility and pairing calculations

We assume that the interaction part of the full model Hamiltonian is given by the multi-orbital Hubbard interaction. Together with the kinetic part determined from the Wannier function calculation, the full Hamiltonian is given by

$$\begin{aligned} H &= H_0 + H_{\text{int}} \\ &= - \sum_{i,j,s,p,\sigma} t_{ij}^{sp} c_{is\sigma}^\dagger c_{jp\sigma} + U \sum_{i,l} n_{i\uparrow} n_{i\downarrow} \\ &\quad + \frac{U'}{2} \sum_{i,s,p \neq s} n_{is} n_{ip} - \frac{J}{2} \sum_{i,s,p \neq s} \mathbf{S}_{is} \cdot \mathbf{S}_{ip} \\ &\quad + \frac{J'}{2} \sum_{i,s,p \neq s,\sigma} c_{is\sigma}^\dagger c_{is\bar{\sigma}}^\dagger c_{ip\bar{\sigma}} c_{ip\sigma}. \end{aligned} \quad (2)$$

The number operator is given by  $n_{is\sigma} = c_{is\sigma}^\dagger c_{is\sigma}$  and  $\mathbf{S}_s = \frac{1}{2} \sum_{\alpha\beta} c_{s\alpha}^\dagger \boldsymbol{\sigma}_{\alpha\beta} c_{s\beta}$  is a spin operator with orbital index denoted by  $s$  and the spins of electrons denoted by  $\alpha$  and  $\beta$ . The interaction parameters are the intra-orbital Coulomb repulsion ( $U$ ), the inter-orbital Coulomb repulsion ( $U'$ ), the Hund's rule coupling ( $J$ ) and the pair-hopping term ( $J'$ ). For the values of these parameters we make an assumption that is consistent with the existing literature:  $U = 1.25 \text{ eV}$ ,  $U' = U/2$ ,  $J = J' = U/4$ .

Our aim is now to calculate the two-particle pairing vertex within the random phase approximation (RPA)<sup>45–47</sup>. We first calculate the non-interacting susceptibility  $\chi_{st}^{pq}(\mathbf{q})$  as a function of momentum, but at vanishing excitation frequency (static limit).

$$\begin{aligned} \chi_{st}^{pq}(\mathbf{q}) &= - \sum_{\mathbf{k},l,m} a_l^{p*}(\mathbf{k}) a_l^t(\mathbf{k}) a_m^{s*}(\mathbf{k} + \mathbf{q}) a_m^q(\mathbf{k} + \mathbf{q}) \\ &\quad \times \frac{n_F(E_l(\mathbf{k})) - n_F(E_m(\mathbf{k} + \mathbf{q}))}{E_l(\mathbf{k}) - E_m(\mathbf{k} + \mathbf{q})} \end{aligned} \quad (3)$$

Matrix elements  $a_l^t(\mathbf{k})$  resulting from the diagonalization of the kinetic Hamiltonian  $H_0$  connect orbital and band space denoted by indices  $t$  and  $l$  respectively. The energies  $E_l$  are the eigenvalues of  $H_0$  and  $n_F(E)$  is the Fermi function. In our calculation both  $\mathbf{q}$  and  $\mathbf{k}$  run over uniform grids spanning the reciprocal unit cell. Temperature enters the calculation through the Fermi functions.

The denominator of the fraction in Eq. 3 can in principle vanish whenever the band energies  $E_l$  and  $E_m$  become equal. However, it can be shown easily using l'Hospital's rule that this does not lead to a diverging susceptibility.

$$\begin{aligned} &\lim_{E_l \rightarrow E_m} \frac{n_F(E_l(\mathbf{k} + \mathbf{q})) - n_F(E_m(\mathbf{k}))}{E_l(\mathbf{k} + \mathbf{q}) - E_m(\mathbf{k})} \\ &= -\beta \frac{e^{\beta E_l}}{(e^{\beta E_l} + 1)^2} \end{aligned} \quad (4)$$

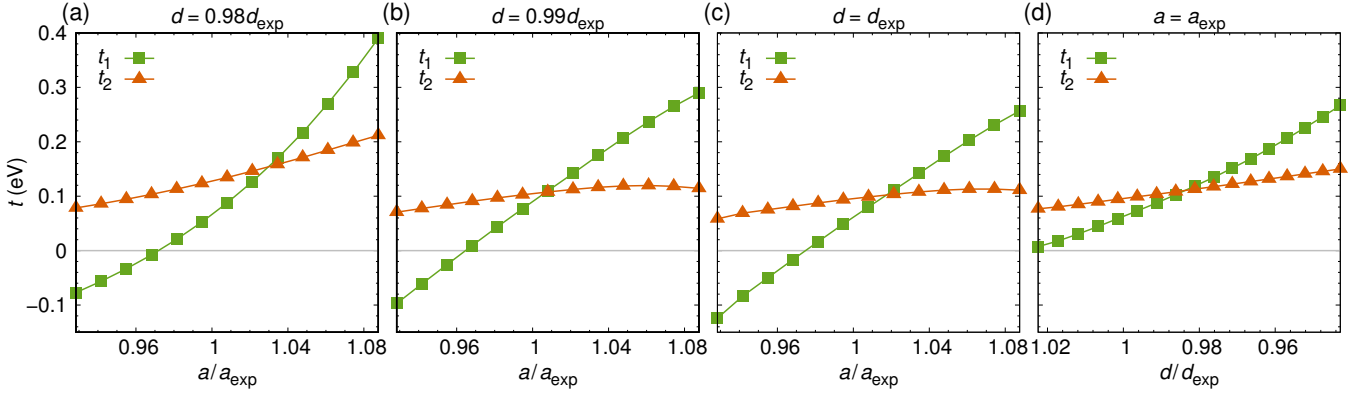


FIG. 6. (Color online) Nearest ( $t_1$ ) and next-nearest ( $t_2$ ) neighbor hopping parameters in the Fe  $3d_{xy}$  orbitals (a) as function of lattice parameters  $a$  at fixed iron-selenium distance (a)  $d_{\text{Fe-Se}} = 2.35 \text{ \AA} = 0.98d_{\text{exp}}$ , (b)  $d_{\text{Fe-Se}} = 2.37 \text{ \AA} = 0.99d_{\text{exp}}$  and (c)  $d_{\text{Fe-Se}} = 2.393 \text{ \AA} \equiv d_{\text{exp}}$ . (d) The hoppings at fixed lattice parameter  $a = 3.76988 \text{ \AA} \equiv a_{\text{exp}}$  and varied iron-selenium distance  $d_{\text{Fe-Se}}$ .

Here,  $\beta$  denotes the inverse temperature  $\beta = (k_B T)^{-1}$ . In practice we use this formula if the magnitude of the denominator falls below a certain threshold (e.g.  $10^{-7} \text{ eV}$ ).

The observable non-interacting susceptibility is defined as the sum over all elements  $\chi_{aa}^{bb}$  of the full tensor.

$$\chi(\mathbf{q}) = \frac{1}{2} \sum_{a,b} \chi_{aa}^{bb}(\mathbf{q}) \quad (5)$$

Within the random phase approximation the charge and spin susceptibilities can be calculated from the non-interacting susceptibility using inversion formulas involving the constant tensors  $U^c$  and  $U^s$  for the charge and spin channel, respectively.

$$[(\chi^s(\mathbf{q}))_{st}^{pq}]^{-1} = [\chi_{st}^{pq}(\mathbf{q})]^{-1} - (U^s)_{st}^{pq} \quad (6a)$$

$$[(\chi^c(\mathbf{q}))_{st}^{pq}]^{-1} = [\chi_{st}^{pq}(\mathbf{q})]^{-1} + (U^c)_{st}^{pq} \quad (6b)$$

Following Ref. 45 the interaction tensors for the multi-orbital Hubbard model are given by

$$\begin{aligned} (U^c)_{aa}^{aa} &= U & (U^c)_{aa}^{bb} &= 2U' \\ (U^c)_{ab}^{ab} &= \frac{3}{4}J - U' & (U^c)_{ab}^{ba} &= J' \\ (U^s)_{aa}^{aa} &= U & (U^s)_{aa}^{bb} &= \frac{1}{2}J \\ (U^s)_{ab}^{ab} &= \frac{1}{4}J + U' & (U^s)_{ab}^{ba} &= J'. \end{aligned} \quad (7)$$

The two-particle pairing vertex in the spin-singlet channel can be constructed from the charge and spin susceptibilities and the constant interaction tensors<sup>45</sup>.

$$\begin{aligned} &(\Gamma^s)_{st}^{pq}(\mathbf{k}, \mathbf{k}') \\ &= \left[ \frac{3}{2} U^s \chi^s(\mathbf{k} \pm \mathbf{k}') U^s - \frac{1}{2} U^c \chi^c(\mathbf{k} \pm \mathbf{k}') U^c \right]_{st}^{pq} \\ &+ \frac{1}{2} [U^c + U^s]_{st}^{pq} \end{aligned} \quad (8)$$

The previously calculated two-particle pairing vertex in orbital space is projected into band space using the matrix elements  $a_l^i(\mathbf{k})$  of the kinetic Hamiltonian.

$$\begin{aligned} &\Gamma_{mn}(\mathbf{k}, \mathbf{k}') \\ &= \text{Re} \left[ \sum_{pq, st} a_m^{p*}(\mathbf{k}) a_n^{t*}(-\mathbf{k}) (\Gamma^s)_{st}^{pq}(\mathbf{k}, \mathbf{k}') a_n^q(\mathbf{k}') a_n^s(-\mathbf{k}') \right] \end{aligned} \quad (9)$$

Restricting the momenta  $\mathbf{k}$  and  $\mathbf{k}'$  in the pairing vertex to points  $\mathbf{k}_m$  and  $\mathbf{k}_n$  on the discretized Fermi surface, we can write down an effective eigenvalue equation.

$$\lambda g(\mathbf{k}_n) = - \sum_{\mathbf{k}_m} \frac{\Gamma(\mathbf{k}_m, \mathbf{k}_n)}{\hbar |\mathbf{v}(\mathbf{k}_m)|} g(\mathbf{k}_m) \quad (10)$$

Diagonalization of the kernel yields the symmetry eigenfunctions  $g(\mathbf{k}_n)$  and corresponding eigenvalues  $\lambda$ , which characterize the strength of the electron pairing.

In our calculations the three-dimensional Fermi surface is discretized using about 1000  $\mathbf{k}$ -points. The susceptibility is calculated on a  $30 \times 30 \times 10$   $\mathbf{k}$ -point grid at an inverse temperature of  $\beta = 40 \text{ eV}^{-1}$ .

### III. RESULTS

#### A. Electronic structure

We investigated the electronic structure as a function of the lattice parameter  $a$  and the iron-selenium distance  $d_{\text{Fe-Se}}$ . An overview of electronic bandstructures as a function of the  $a$  lattice parameter with varied distance  $d_{\text{Fe-Se}}$  is shown in Fig. 2, while Fig. 3 shows a scan of iron-selenium distances  $d_{\text{Fe-Se}}$  in a different range around the experimental value, keeping constant the lattice parameter  $a$ . Corresponding Fermi surfaces are shown in Figs. 4 and 5.



At small lattice parameters  $a = 0.93a_{\text{exp}}$  the Brillouin zone comprises two hole pockets and two electron pockets [Fig. 2 (a)-(c) and Fig. 4 (a)-(c)]. The iron-selenium distance  $d_{\text{Fe-Se}}$  hardly influences the electronic structure. An expansion of the iron lattice to  $a = 1.01a_{\text{exp}}$  decreases the size of the Fe  $3d_{xy}$  hole pockets and brings up a new Fe  $3d_{xz/yz}$  hole pocket [Fig. 2 (d)-(f) and Fig. 4 (d)-(f)]. The relative size is somewhat influenced by  $d_{\text{Fe-Se}}$ . At  $a = 4.1 \text{ \AA} = 1.09a_{\text{exp}}$  all Fermi surface pockets are small. The relative position of Fe  $3d_{xy}$  and Fe  $3d_{z^2}$  bands at the M= $(\pi, \pi, 0)$  point is controlled by  $d_{\text{Fe-Se}}$ . Around the experimental value of  $d_{\text{Fe-Se}}$  hole-pockets of Fe  $3d_{z^2}$  character emerge around M [Fig. 2 (h)-(i) and Fig. 4 (h)-(i)].

When tuning only  $d_{\text{Fe-Se}}$  and keeping  $a$  at the experimental value, the picture is similar (Figs. 3 and 5). As  $d_{\text{Fe-Se}}$  decreases, the two present Fe  $3d_{xz/yz}$  hole pockets at  $\Gamma=(0,0,0)$  converge in size, while the electron pockets at X= $(\pi,0,0)$  shrink a little. The Fe  $3d_{xy}$  hole pockets around M finally disappear, so that one ends up with a Fermi surface with very small electron and hole pockets [see Figs. 3 (c) and 5 (c)].

These observations can be directly related to the hopping parameters between Fe  $3d_{xy}$  orbitals. While the next-nearest-neighbor hopping  $t_2$  is roughly constant, the nearest-neighbor hopping  $t_1$  is strongly influenced by the lattice expansion (see Fig. 6), which explains the strong influence of lattice parameters on the Fe  $3d_{xy}$  hole pocket. Intuitively, one would expect that nearest-neighbor hopping  $t_1$  increases upon compression, while we find a strong decrease.

The reason for this behavior has been exhaustively assessed in Ref. 48 (see in particular Fig. 4 therein). In summary, the nearest-neighbor hopping  $t_1$  is the sum of direct Fe-Fe hopping paths and indirect Fe-Se-Fe paths. Direct and indirect contributions to  $t_1$  have opposite signs. At equilibrium lattice parameters the indirect hopping contributions to  $t_1$  dominate. Therefore, as direct Fe-Fe hopping is enhanced upon compression,  $t_1$  counter-intuitively decreases and even changes sign in the extreme compressed regime [see Fig. 6 (a-c)]. The next-nearest neighbor hopping  $t_2$ , however, is hardly affected by compression, since it depends in first approximation only on the Fe-Se-Fe hopping. This picture is clearly consistent also with Fig. 6 (d), where  $t_1$  decreases as the Fe-Se distance is increased. In this case direct Fe-Fe hoppings stay constant, while indirect hopping via Se decreases due to the larger Fe-Se distance, so that  $t_1$  finally vanishes in the most expanded case we investigated. The importance of the balance of  $t_1$  and  $t_2$  for superconductivity in iron-based materials has been assessed in previous publications<sup>48,49</sup>.

### B. Non-interacting observable susceptibility

The non-interacting susceptibility is calculated from Eqs. 3 and 5. The static susceptibility on the high-

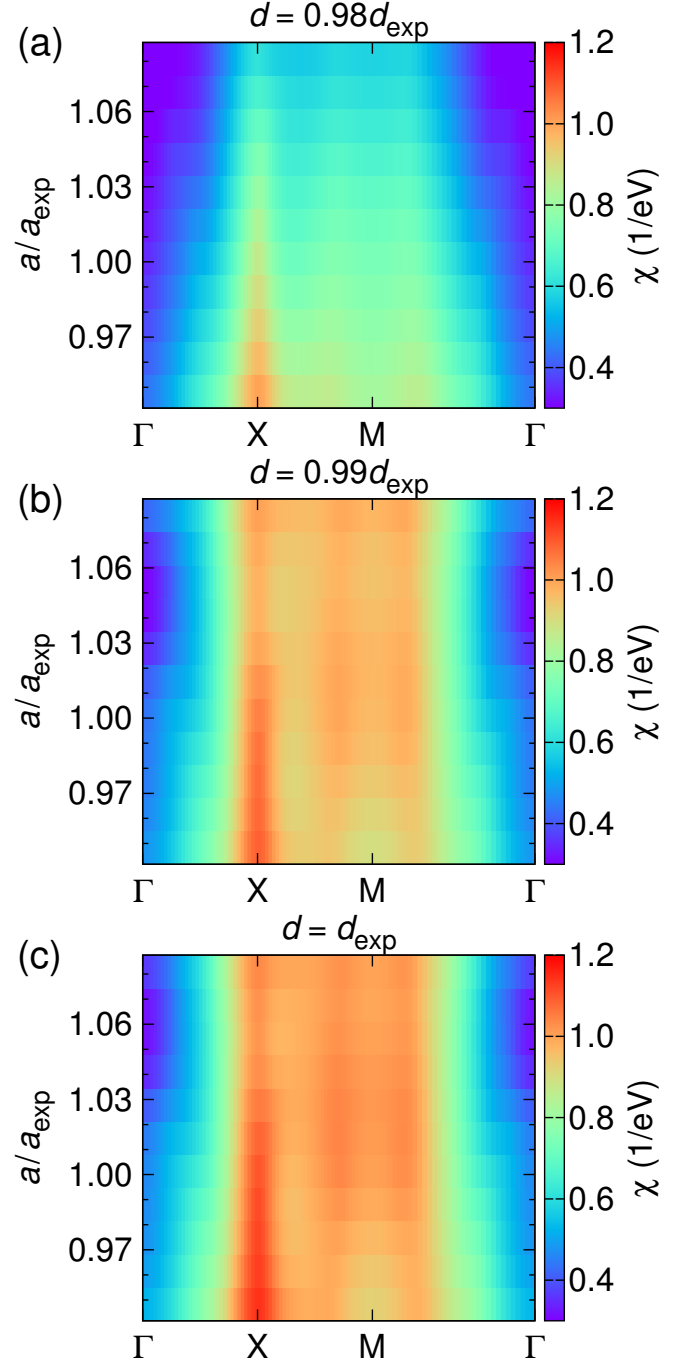


FIG. 7. (Color online) Static susceptibility on a high-symmetry path as a function of the lattice parameter  $a$ . The iron-selenium distance is kept fixed at (a)  $d_{\text{Fe-Se}}=0.98d_{\text{Fe-Se exp}}$ , (b)  $d_{\text{Fe-Se}}=0.99d_{\text{Fe-Se exp}}$  and (c)  $d_{\text{Fe-Se}}=d_{\text{Fe-Se exp}}$ .

symmetry path  $\Gamma$ -X-M- $\Gamma$  is shown in Fig. 7 as a function of the  $a$  lattice parameter and  $d_{\text{Fe-Se}}$ . In Fig. 8 the static susceptibility is shown as a function of  $d_{\text{Fe-Se}}$  in a somewhat different range, but at constant lattice parameter  $a_{\text{exp}}$ .

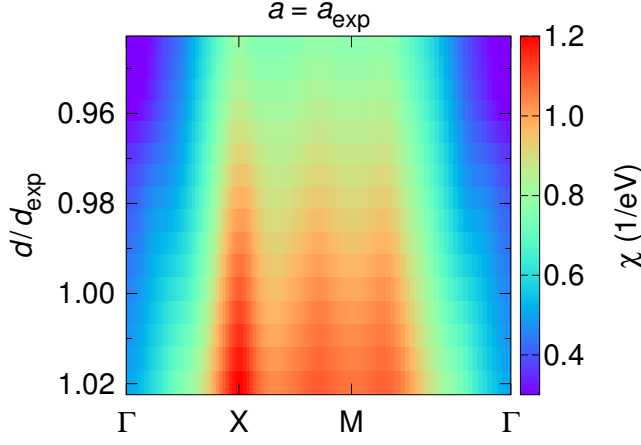


FIG. 8. (Color online) Static susceptibility on a high-symmetry path as a function of  $d_{\text{Fe-Se}}$  at fixed lattice parameter  $a = a_{\text{exp}}$ .

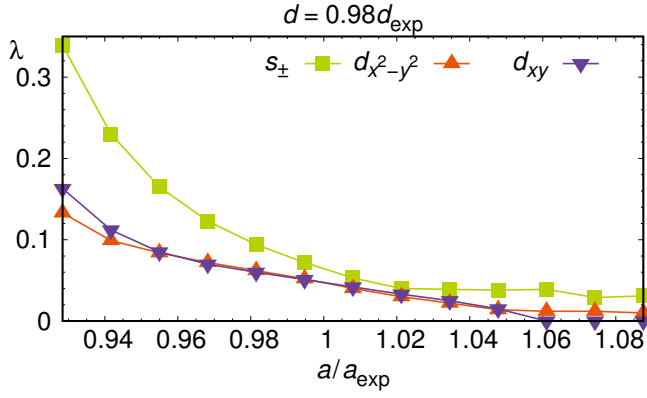


FIG. 9. (Color online) Pairing eigenvalues  $\lambda$  as a function of the lattice parameter  $a$  at fixed iron-selenium distance  $d = 0.98d_{\text{Fe-Se exp}}$ .

A decrease of  $d_{\text{Fe-Se}}$  at constant  $a_{\text{exp}}$  weakens the susceptibility (Fig. 8), while an increase in  $d_{\text{Fe-Se}}$  strongly enhances the susceptibility. A change in the lattice parameter  $a$  (Fig. 7) produces more interesting behavior: Except at  $d_{\text{Fe-Se}} = 0.98d_{\text{Fe-Se exp}}$  only the susceptibility at the X point is selectively weakened by the lattice expansion, while the susceptibility around the M point is enhanced. Since the static susceptibility at the X point is associated with stripe antiferromagnetism, while the static susceptibility at M is associated with checkerboard antiferromagnetism, this nontrivial behavior of the static susceptibility might be important for extremely stretched films of iron selenide, where stripe AFM order can be expected to compete with checkerboard AFM order.<sup>50</sup>

In the following we explain the behavior of the static susceptibility based on the evolution of the electronic bandstructures and Fermi surfaces. The monotonous decrease of the susceptibility for constant lattice parameter  $a$  and varied  $d_{\text{Fe-Se}}$  (Fig. 8) is due to the vanishing of the Fe  $3d_{xy}$  hole pocket at the M point as shown in Figs. 3

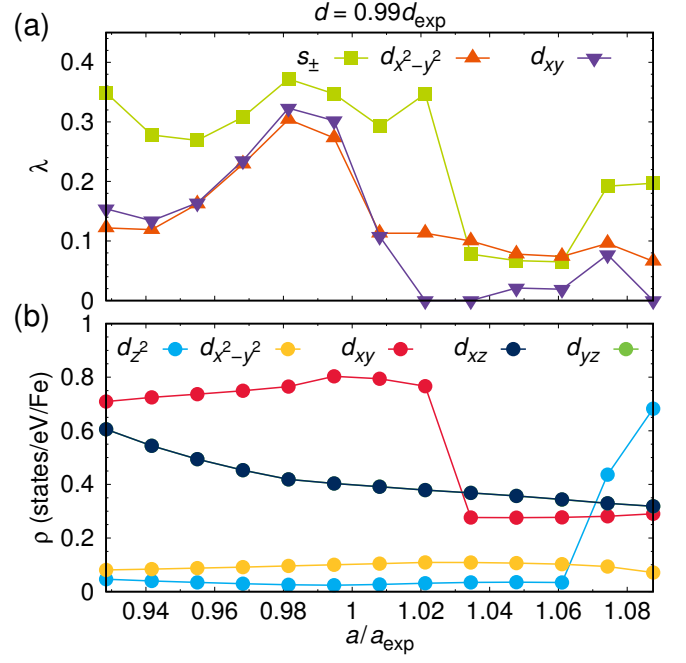


FIG. 10. (Color online) (a) Pairing eigenvalues  $\lambda$  and (b) orbital-resolved density of states  $\rho$  at the Fermi level as a function of the lattice parameter  $a$  at fixed iron-selenium distance  $d = 0.99d_{\text{Fe-Se exp}}$ .

and 5. The shape of the Fermi surface otherwise remains unaltered, so that only a quantitative decrease of the susceptibility is observed due to the reduced spectral weight at the Fermi level. The same is true for varied lattice parameter  $a$  and  $d_{\text{Fe-Se}} = 0.98d_{\text{Fe-Se exp}}$  [compare Figs. 2 (a,d,g) to Fig. 3 and Figs. 4 (a,d,g) to Fig. 5]. Likewise Figs. 6 (a) and (d) contain similar trends for the hopping parameters between Fe  $3d_{xy}$  orbitals.

Furthermore, while the reduction of the susceptibility at the X point is obvious for constant  $d_{\text{Fe-Se}}$  at varied lattice parameters  $a$  (see Fig. 7), the increased susceptibility at the M point is the outstanding non-trivial feature upon lattice expansion. Also here we observe the Fe  $3d_{xy}$  hole pocket vanish, but the electron pockets located around X and the hole pockets in the Brillouin zone center contract notably [see Figs. 2 (h-i) and 4 (h-i)]. This means that the increased susceptibility at M is due to enhanced scattering processes involving the contracted Fe  $3d_{xy}$  electron pockets. This is also made plausible by the location of maxima in susceptibility in Fig. 7, which seem to converge towards the M point with enlarged lattice parameter  $a$ , i.e. when the electron pockets contract.

### C. Symmetry and strength of electron pairing

Several scans of the pairing strength and symmetries are shown in Figs. 9, 10, 11, 12 and 13. The pairing symmetries with largest eigenvalues can be characterized as  $s_{\pm}$  (sign-changing  $s$ -wave),  $d_{x^2-y^2}$  and  $d_{xy}$ . These

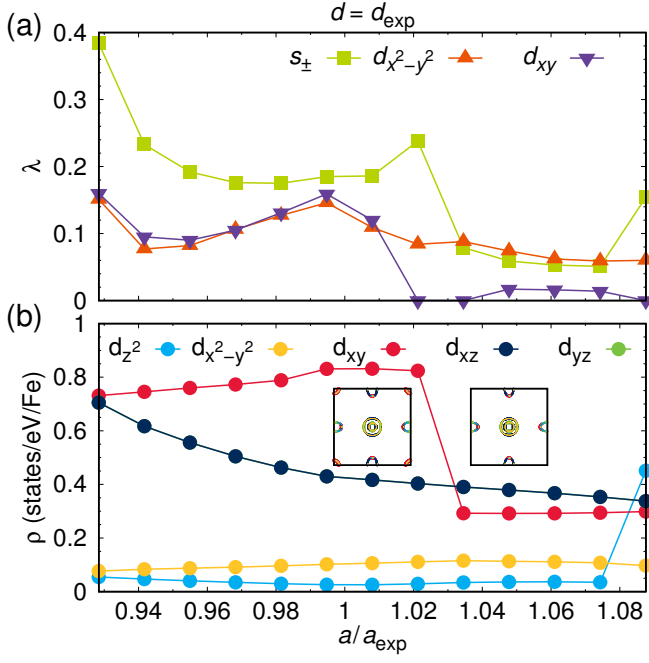


FIG. 11. (Color online) (a) Pairing eigenvalues  $\lambda$  and (b) orbital-resolved density of states  $\rho$  at the Fermi level as a function of the lattice parameter  $a$  at fixed iron-selenium distance  $d_{\text{Fe-Se}} = d_{\text{Fe-Se exp}}$ .

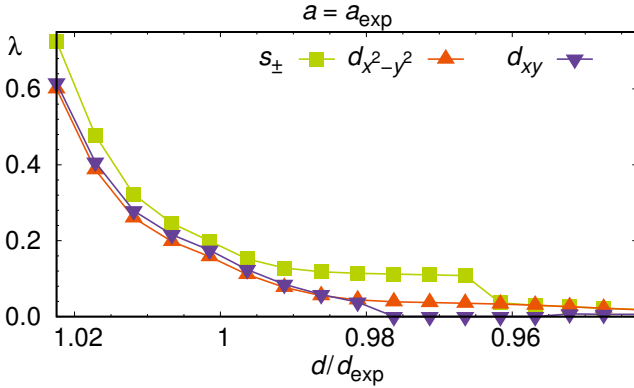


FIG. 12. (Color online) Pairing eigenvalues  $\lambda$  as a function of the iron-selenium distance  $d_{\text{Fe-Se}}$  at fixed lattice parameter  $a = a_{\text{exp}}$ .

are the symmetry eigenfunctions that usually compete in iron-based superconductors.

For small  $d_{\text{Fe-Se}} = 0.98d_{\text{Fe-Se exp}}$  at varied  $a$  and for constant  $a$  at varied  $d_{\text{Fe-Se}}$  the results do not contain much structure. The pairing eigenvalues monotonously decrease with increased  $a$  and with decreased  $d_{\text{Fe-Se}}$  (see Figs. 9 and 12). For larger  $d_{\text{Fe-Se}}$ , the pairing strength and the symmetry of the leading solution in the pairing eigenproblem on the lattice parameter  $a$  mirrors the non-trivial results we obtained for the susceptibility (see Figs. 10 and 11).

For varied lattice parameter  $a$  and constant iron-

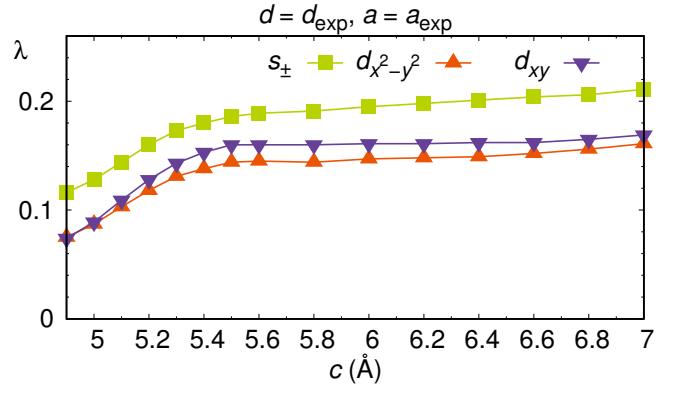


FIG. 13. (Color online) Pairing eigenvalues  $\lambda$  as a function of the lattice parameter  $c$  at fixed lattice parameter  $a = a_{\text{exp}}$  and fixed iron-selenium distance  $d_{\text{Fe-Se}} = d_{\text{Fe-Se exp}}$ .

selenium distance  $d_{\text{Fe-Se}} \geq 0.99d_{\text{Fe-Se exp}}$  we observe a breakdown of the  $s_{\pm}$  solution (see Figs. 10 and 11) at the Lifshitz transition, where the Fe  $3d_{xy}$  hole pocket disappears, as clearly indicated by the jump in the Fe  $3d_{xy}$  density of states at the Fermi level (see also Fig. 4). Just before the breakdown, the  $s_{\pm}$  pairing is quite strongly enhanced, probably because of the enhanced density of states at the Fermi level contributed by the upper edge of the hole band.

Before the breakdown of  $s_{\pm}$  pairing, the  $d_{xy}$  pairing state is already completely suppressed. This is the case because a nodal  $s_{\pm}$  state can also accommodate susceptibilities with wave vector around the M point via the introduction of nodes into the order parameter, while the inclusion of additional nodes is very hard for the  $d_{xy}$  state. However, the  $d_{x^2-y^2}$  state takes the lead when the Fe  $3d_{xy}$  hole pocket has disappeared. This fact relates directly to the emergent peak in the susceptibility at the M point and the strong decrease at the X point. Note, however, that the pairing strength is severely decreased after the Lifshitz transition.

In the intermediate region there is strong competition between  $d_{xy}$  and  $d_{x^2-y^2}$  pairing for the first subleading solution, while  $s_{\pm}$  remains the leading solution. The intermediate enhancement of  $d_{xy}$  pairing occurs whenever the geometry of the Fe  $3d_{xz/yz}$  hole and electron pockets matches well. In this case, the  $s_{\pm}$  pairing state can, however, avoid nodes on the Fermi surface altogether and consequently takes the lead. Platt *et al.* explain this general phenomenon in terms of optimization of the condensation energy<sup>51</sup>.

Remarkably, in Fig 12 an expansion of  $d_{\text{Fe-Se}}$  leads to a similarly strong increase of pairing eigenvalues regardless of the associated symmetry eigenfunction. This is a consequence of the overall strongly enhanced susceptibility we observed in Fig. 8, which does have a maximum at the X point, but less well separated from other peaks than in Fig. 7. Therefore, it is likely that a strong degeneracy of different magnetic states is present under expansion of  $d_{\text{Fe-Se}}$ . The presence of magnetic degeneracy should sup-



press possible competing long range magnetic order and is likely beneficial for superconductivity if the degeneracy is between pairing-promoting states. To elucidate this issue, DFT calculations for different magnetic states could be instructive, but are beyond the scope of the present paper.

A scan of the dependence on the  $c$  lattice parameter is shown in Fig. 13, which is reminiscent of the plot by Noji *et al.*<sup>28</sup> that showed a levelling-off of the superconducting transition temperature  $T_c$  in certain intercalates when the distance between FeSe layers is increased. However, the critical length is somewhat smaller here than in typical intercalates, probably because in our model study presented here we do not actually intercalate anything in between of the FeSe layers, but leave the space in between as vacuum. Note that the actual behavior of those intercalates is not only a function of layer distance, but also crucially depends on electron doping<sup>23,24,49</sup>.

As a final note, FeS<sup>16</sup> has lattice parameters  $a = 3.6802$  Å and  $d_{\text{Fe-S}} = 2.235$  Å with relations relative to the experimental values of FeSe,  $a_{\text{FeS}}/a_{\text{FeSe}} = 0.98$  and  $d_{\text{Fe-S}}/d_{\text{Fe-Se}} = 0.93$ . This corresponds to an extremely compressed case, further reducing the  $a$  parameter in Figs. 3 (c) and 5 (c) (see Ref. 18). Extrapolating the trends of Fig. 12 (a) and Fig. 13 it is to be expected that the susceptibility for this case will be rather featureless which would further reduce  $T_c$ . Actually,  $T_c$  in FeS is 4 K.

## IV. SUMMARY

We have discussed that the underlying electronic structure of iron selenide depends both on the lattice spacing and the iron-selenium distance in a nontrivial way, leading to complex behavior of non-interacting susceptibility and electron pairing, with several competing channels. Our main observations are: (i) Expansion of the Fe square lattice parameter at constant Fe-Se distance should enhance  $T_c$  up to a point before a switch of superconducting order parameter from  $s_{\pm}$  to  $d_{x^2-y^2}$  occurs. (ii) Increasing Fe-Se distance at constant Fe square lattice parameter  $a$  should enhance  $T_c$ . (iii) Increasing the  $c$  lattice parameter at constant experimental  $d_{\text{Fe-Fe}}$  and  $d_{\text{Fe-Se}}$  distances (i.e. increasing the van der Waals gap) slightly increases  $T_c$ . (iv) Compression of the Fe-Fe square lattice at compressed Fe-Se distance significantly enhances  $T_c$ . Observation (iii) is essentially known from charge neutral FeSe intercalates. Observation (iv) is very consistent with the well known pressure enhancement of  $T_c$ <sup>52</sup>. However, observations (i) and (ii) could lead to new design ideas.

## ACKNOWLEDGMENTS

The authors acknowledge support from the German Research Foundation (Deutsche Forschungsgemeinschaft). Furthermore, the authors would like to thank Matthew D. Watson, Amalia I. Coldea, Steffen Backes, Andreas Kreisel and Peter J. Hirschfeld for helpful discussions.

---

\* Present address: Lucht Probst Associates, Große Gallusstraße 9, 60311 Frankfurt am Main, Germany; daniel.guterding@gmail.com

<sup>1</sup> F.-C. Hsu, J.-Y. Luo, K.-W. Yeh, T.-K. Chen, T.-W. Huang, P. M. Wu, Y.-C. Lee, Y.-L. Huang, Y.-Y. Chu, and D.-C. Yan, and M.-K. Wu, *Superconductivity in the PbO-type structure  $\alpha$ -FeSe*, Proc. Natl. Acad. Sci. U.S.A. **105**, 14262 (2008).

<sup>2</sup> see for a review A. Coldea and M. D. Watson, *The key ingredients of the electronic structure of FeSe*, arXiv:1706.00338 (unpublished).

<sup>3</sup> see for instance: A. E. Böhmer and C. Meingast, *Electronic nematic susceptibility of iron-based superconductors*, C. R. Physique **17**, 90 (2016).

<sup>4</sup> J. K. Glasbrenner, I. I. Mazin, H. O. Jeschke, P. J. Hirschfeld, R.M. Fernandes, and R. Valentí, *Effect of magnetic frustration on nematicity and superconductivity in iron chalcogenides*, Nat. Phys. **11**, 953 (2015).

<sup>5</sup> F. Wang, S.A. Kivelson, and D.-H. Lee, *Nematicity and quantum paramagnetism in FeSe*, Nat. Phys. **11**, 959 (2015).

<sup>6</sup> A. V. Chubukov, M. Khodas, and R. M. Fernandes, *Magnetism, Superconductivity, and Spontaneous Orbital Order in Iron-Based Superconductors: Which Comes First and*

*Why?*, Phys. Rev. X **6**, 041045 (2016).

<sup>7</sup> Y. Yamakawa, S. Onari, and H. Kontani, *Nematicity and magnetism in FeSe and other families of Fe-based superconductors* Phys. Rev. X **6**, 021032 (2016).

<sup>8</sup> L. Fanfarillo, J. Mansart, P. Toulemonde, H. Cercellier, P. Le Fevre, F. Bertran, B. Valenzuela, L. Benfatto, and V. Brouet, *Orbital-dependent Fermi surface shrinking as a fingerprint of nematicity in FeSe*, Phys. Rev. B **94**, 155138 (2016).

<sup>9</sup> D. D. Scherer, A. C. Jacko, Ch. Friedrich, E. Sasioglu, S. Blügel, R. Valentí, and B. M. Andersen, *Interplay of nematic and magnetic orders in FeSe under pressure*, Phys. Rev. B **95**, 094504 (2017).

<sup>10</sup> D. Liu, W. Zhang, D. Mou, J. He, Y.-B. Ou, Q.-Y. Wang, Z. Li, L. Wang, L. Zhao, S. He, Y. Peng, X. Liu, C. Chen, L. Yu, G. Liu, X. Dong, J. Zhang, C. Chen, Z. Xu, J. Hu, X. Chen, X. Ma, Q. Xue, and X. J. Zhou, *Electronic origin of high-temperature superconductivity in single-layer FeSe superconductor*, Nat. Commun. **3**, 931 (2012).

<sup>11</sup> S. Tan, Y. Zhang, M. Xia, Z. Ye, F. Chen, X. Xie, R. Peng, D. Xu, Q. Fan, H. Xu, J. Jiang, T. Zhang, X. Lai, T. Xiang, J. Hu, B. Xie, and D. Feng, *Interface-induced superconductivity and strain-dependent spin density waves in FeSe/SrTiO<sub>3</sub> thin films*, Nat. Mater. **12**, 634 (2013).

- <sup>12</sup> J.-F. Ge, Z.-L. Liu, C. Liu, C.-L. Gao, D. Qian, Q.-K. Xue, Y. Liu, and J.-F. Jia, *Superconductivity above 100 K in single-layer FeSe films on doped SrTiO<sub>3</sub>*, Nat. Mater. **14**, 285 (2014).
- <sup>13</sup> M. D. Watson, T. K. Kim, A. A. Haghighirad, S. F. Blake, N. R. Davies, M. Hoesch, T. Wolf, A. I. Coldea, *Suppression of orbital ordering by chemical pressure in FeSe<sub>1-x</sub>S<sub>x</sub>*, Phys. Rev. B **92**, 121108 (2015).
- <sup>14</sup> A. I. Coldea, S. F. Blake, S. Kasahara, A. A. Haghighirad, M. D. Watson, W. Knafo, E. S. Choi, A. McCollam, P. Reiss, T. Yamashita, M. Bruma, S. Speller, Y. Matsuda, T. Wolf, T. Shibauchi, and A. J. Schofield, *Evolution of the Fermi surface of the nematic superconductors FeSe<sub>1-x</sub>S<sub>x</sub>*, arXiv:1611.07424 (unpublished).
- <sup>15</sup> K. Matsuura, Y. Mizukami, Y. Arai, Y. Sugimura, N. Maejima, A. Machida, T. Watanuki, T. Fukuda, T. Yajima, Z. Hiroi, K. Y. Yip, Y. C. Chan, Q. Niu, S. Hosoi, K. Ishida, K. Mukasa, T. Watashige, S. Kasahara, J.-G. Cheng, S. K. Goh, Y. Matsuda, Y. Uwatoko, and T. Shibauchi, *Maximizing T<sub>c</sub> by tuning nematicity and magnetism in FeSe<sub>1-x</sub>S<sub>x</sub> superconductors*, arXiv:1704.02057 (unpublished).
- <sup>16</sup> X. Lai, H. Zhang, Y. Wang, X. Wang, X. Zhang, J. Lin, and F. Huang, *Observation of Superconductivity in Tetragonal FeS*, J. Am. Chem. Soc. **137**, 10148 (2015).
- <sup>17</sup> T. P. Ying, X. F. Lai, X. C. Hong, Y. Xu, L. P. He, J. Zhang, M. X. Wang, Y. J. Yu, F. Q. Huang, and S. Y. Li, *Nodal superconductivity in FeS: Evidence from quasiparticle heat transport*, Phys. Rev. B **94**, 100504(R) (2016).
- <sup>18</sup> C. Tresca, G. Giovanetti, M. Capone, and G. Profeta, *Electronic properties of superconducting FeS*, Phys. Rev. B **95**, 205117 (2017).
- <sup>19</sup> S. J. Sedlmaier, S. J. Cassidy, R. G. Morris, M. Drakopoulos, C. Reinhard, S. J. Moorhouse, D. O'Hare, P. Manuel, D. Khalyavin, and S. J. Clarke, *Ammonia-Rich High-Temperature Superconducting Intercalates of Iron Selenide Revealed through Time-Resolved in Situ Xray and Neutron Diffraction*, J. Am. Chem. Soc. **136**, 630 (2014).
- <sup>20</sup> M. Burrard-Lucas, D. G. Free, S. J. Sedlmaier, J. D. Wright, S. J. Cassidy, Y. Hara, A. J. Corkett, T. Lancaster, P. J. Baker, S. J. Blundell, and S. J. Clarke, *Enhancement of the superconducting transition temperature of FeSe by intercalation of a molecular spacer layer*, Nat. Mater. **12**, 15 (2013).
- <sup>21</sup> X. Dong, H. Zhou, H. Yang, J. Yuan, K. Jin, F. Zhou, D. Yuan, L. Wei, J. Li, X. Wang, G. Zhang, and Z. Zhao, *Phase Diagram of (Li<sub>1-x</sub>Fe<sub>x</sub>)OHFeSe: A Bridge between Iron Selenide and Arsenide Superconductors*, J. Am. Chem. Soc. **137**, 66 (2014).
- <sup>22</sup> J. W. Lynn, X. Zhou, C. K. H. Borg, S. R. Saha, J. Paglione, and E. E. Rodriguez, *Neutron investigation of the magnetic scattering in an iron-based ferromagnetic superconductor*, Phys. Rev. B **92**, 060510(R) (2015).
- <sup>23</sup> F. Hayashi, H. Lei, J. Guo, and H. Hosono, *Modulation Effect of Interlayer Spacing on the Superconductivity of Electron-Doped FeSe-Based Intercalates*, Inorg. Chem. **54**, 3346 (2015).
- <sup>24</sup> H. Sun, D. N. Woodruff, S. J. Cassidy, G. M. Allcroft, S. J. Sedlmaier, A. L. Thompson, P. A. Bingham, S. D. Forder, S. Cartenet, N. Mary, S. Ramos, F. R. Foronda, B. H. Williams, X. Li, S. J. Blundell, and S. J. Clarke, *Soft Chemical Control of Superconductivity in Lithium Iron Selenide Hydroxides Li<sub>1-x</sub>Fe<sub>x</sub>(OH)Fe<sub>1-y</sub>Se*, Inorg. Chem. **54**, 1958 (2015).
- <sup>25</sup> X. F. Lu, N. Z. Wang, H. Wu, Y. P. Wu, D. Zhao, X. Z. Zeng, X. G. Luo, T. Wu, W. Bao, G. H. Zhang, F. Q. Huang, Q. Z. Huang, and X. H. Chen, *Coexistence of superconductivity and antiferromagnetism in (Li<sub>0.8</sub>Fe<sub>0.2</sub>)OHFeSe*, Nat. Mater. **14**, 325 (2015).
- <sup>26</sup> U. Pachmayr, F. Nitsche, H. Luetkens, S. Kamusella, F. Brückner, R. Sarkar, H.-H. Klauss, and D. Johrendt, *Coexistence of 3d-Ferromagnetism and Superconductivity in [(Li<sub>1-x</sub>Fe<sub>x</sub>)OH](Fe<sub>1-y</sub>Li<sub>y</sub>)Se*, Angew. Chem. Int. Ed. **54**, 293 (2015).
- <sup>27</sup> J. Guo, S. Jin, G. Wang, S. Wang, K. Zhu, T. Zhou, M. He, and X. Chen, *Superconductivity in the iron selenide K<sub>x</sub>Fe<sub>2</sub>Se<sub>2</sub> (0 ≤ x ≤ 1.0)*, Phys. Rev. B **82**, 180520 (2010).
- <sup>28</sup> T. Noji, T. Hatakeda, S. Hosono, T. Kawamata, M. Kato, and Y. Koike, *Synthesis and post-annealing effects of alkaline-metal-ethylenediamineintercalated superconductors A<sub>x</sub>(C<sub>2</sub>H<sub>8</sub>N<sub>2</sub>)<sub>y</sub>Fe<sub>2-z</sub>Se<sub>2</sub> (A = Li, Na) with T<sub>c</sub> = 45 K*, Physica C **504**, 8 (2014).
- <sup>29</sup> S. Hosono, T. Noji, T. Hatakeda, T. Kawamata, M. Kato, and Y. Koike, *New Superconducting Phase of Li<sub>x</sub>(C<sub>6</sub>H<sub>16</sub>N<sub>2</sub>)<sub>y</sub>Fe<sub>2z</sub>Se<sub>2</sub> with T<sub>c</sub> = 41 K Obtained through the Post-Annealing*, J. Phys. Soc. Jpn. **85**, 013702 (2016).
- <sup>30</sup> S. Medvedev, T. M. McQueen, I. A. Troyan, T. Palasyuk, M. I. Eremets, R. J. Cava, S. Naghavi, F. Casper, V. Ksenofontov, G. Wortmann, and C. Felser, *Electronic and magnetic phase diagram of β-Fe<sub>1.01</sub>Se with superconductivity at 36.7 K under pressure*, Nat. Mater. **8**, 630 (2009).
- <sup>31</sup> T. Terashima, N. Kikugawa, S. Kasahara, T. Watashige, T. Shibauchi, Y. Matsuda, T. Wolf, A. E. Boehmer, F. Hardy, C. Meingast, H. v. Loehneysen, and S. Uji, *Pressure-Induced Antiferromagnetic Transition and Phase Diagram in FeSe*, J. Phys. Soc. Jpn. **84**, 063701 (2015).
- <sup>32</sup> M. J. Wang, J. Y. Luo, T. W. Huang, H. H. Chang, T. K. Chen, F. C. Hsu, C. T. Wu, P. M. Wu, A. M. Chang, and M. K. Wu, *Crystal Orientation and Thickness Dependence of the Superconducting Transition Temperature of Tetragonal FeSe<sub>1-x</sub> Thin Films*, Phys. Rev. Lett. **103**, 117002 (2009).
- <sup>33</sup> Y. F. Nie, E. Brahimi, J. I. Budnick, W. A. Hines, M. Jain, and B. O. Wells, *Suppression of superconductivity in FeSe films under tensile strain*, Appl. Phys. Lett. **94**, 242505 (2009).
- <sup>34</sup> H. Hiramatsu, T. Katase, T. Kamiya, and H. Hosono, *Thin Film Growth and Device Fabrication of Iron-Based Superconductors*, J. Phys. Soc. Jpn. **81**, 011011 (2012).
- <sup>35</sup> B. Lei, J. H. Cui, Z. J. Xiang, C. Shang, N. Z. Wang, G. J. Ye, X. G. Luo, T. Wu, Z. Sun, and X. H. Chen, *Evolution of High-Temperature Superconductivity from a Low-T<sub>c</sub> Phase Tuned by Carrier Concentration in FeSe Thin Flakes*, Phys. Rev. Lett. **116**, 077002 (2016).
- <sup>36</sup> M. Aichhorn, S. Biermann, T. Miyake, A. Georges, and M. Imada, *Theoretical evidence for strong correlations and incoherent metallic state in FeSe*, Phys. Rev. B **82**, 064504 (2010).
- <sup>37</sup> M. D. Watson, S. Backes, A. A. Haghighirad, M. Hoesch, T. K. Kim, A. I. Coldea, and R. Valentí, *Formation of Hubbard-like bands as a fingerprint of strong electron-electron interactions in FeSe*, Phys. Rev. B **95**, 081106(R) (2017).
- <sup>38</sup> D. V. Evtushinsky, M. Aichhorn, Y. Sassa, Z.-H. Liu, J. Maletz, T. Wolf, A. N. Yaresko, S. Biermann, S. V. Borisenko, and B. Büchner, *Direct observation of dispersive lower Hubbard band in iron-based superconductor FeSe*, arXiv:1612.02313 (unpublished).

- <sup>39</sup> S. L. Skornyakov, V. I. Anisimov, D. Vollhardt, and I. Leonov, *Effect of electron correlations on the electronic structure and phase stability of FeSe upon lattice expansion*, Phys. Rev. B **96**, 035137 (2017).
- <sup>40</sup> R. Khasanov, M. Bendele, K. Conder, H. Keller, E. Pomjakushina, and V. Pomjakushin, *Iron isotope effect on the superconducting transition temperature and the crystal structure of FeSe<sub>1-x</sub>*, New J. Phys. **12**, 073024 (2010).
- <sup>41</sup> K. Koepernik and H. Eschrig, *Full-potential nonorthogonal local-orbital minimum-basis band-structure scheme*, Phys. Rev. B **59**, 1743 (1999); <http://www.FPLO.de>
- <sup>42</sup> J. P. Perdew, K. Burke, and M. Ernzerhof, *Generalized Gradient Approximation Made Simple*, Phys. Rev. Lett. **77**, 3865 (1996).
- <sup>43</sup> H. Eschrig and K. Koepernik, *Tight-binding models for the iron-based superconductors*, Phys. Rev. B **80**, 104503 (2009).
- <sup>44</sup> M. Tomić, H. O. Jeschke, and R. Valentí, *Unfolding of electronic structure through induced representations of space groups: Application to Fe-based superconductors*, Phys. Rev. B **90**, 195121 (2014).
- <sup>45</sup> S. Graser, T. A. Maier, P. J. Hirschfeld, and D. J. Scalapino, *Near-degeneracy of several pairing channels in multi-orbital models for the Fe pnictides*, New J. Phys. **11**, 025016 (2009).
- <sup>46</sup> M. Altmeyer, D. Guterding, P. J. Hirschfeld, T. A. Maier, R. Valentí, and D. J. Scalapino, *Role of vertex corrections in the matrix formulation of the random phase approximation for the multi-orbital Hubbard model*, Phys. Rev. B **94**, 214515 (2016).
- <sup>47</sup> D. Guterding, *Microscopic modelling of organic and iron-based superconductors*, PhD thesis, Goethe-Universität Frankfurt am Main, Germany (2017).
- <sup>48</sup> K. Suzuki, H. Usui, S. Iimura, Y. Sato, S. Matsuishi, H. Hosono, and K. Kuroki, *Model of the Electronic Structure of Electron-Doped Iron-Based Superconductors: Evidence for Enhanced Spin Fluctuations by Diagonal Electron Hopping*, Phys. Rev. Lett. **113**, 027002 (2014).
- <sup>49</sup> D. Guterding, H. O. Jeschke, P. J. Hirschfeld, and R. Valentí, *Unified picture of the doping dependence of superconducting transition temperatures in alkali metal/ammonia intercalated FeSe*, Phys. Rev. B **91**, 041112(R) (2015).
- <sup>50</sup> C. Tresca, F. Ricci, and G. Profeta, *Strain effects in monolayer iron-chalcogenide superconductors*, 2D Materials **2**, 015001 (2015).
- <sup>51</sup> Ch. Platt, W. Hanke, and R. Thomale, *Functional renormalization group for multi-orbital Fermi surface instabilities*, Adv. Phys. **62**, 453 (2013).
- <sup>52</sup> Yoshikazu Mizuguchi, Fumiaki Tomioka, Shunsuke Tsuda, Takahide Yamaguchi, and Yoshihiko Takano, *Superconductivity at 27 K in tetragonal FeSe under high pressure*, Appl. Phys. Lett. **93**, 152505 (2008).